Journal of Power Sources 194 (2009) 467–477

Contents lists available at ScienceDirect

Journal of Power Sources

journal homepage: www.elsevier.com/locate/jpowsour

Hysteresis and reaction characterization of methane catalytic partial oxidation on rhodium catalyst

Wei-Hsin Chen [a,*], Tin-Wei Chiu [b], Chen-I Hung [b], Mu-Rong Lin [c]

[a] Department of Greenergy, National University of Tainan, Tainan 700, Taiwan, ROC
[b] Department of Mechanical Engineering, National Cheng Kung University, Tainan 701, Taiwan, ROC
[c] Department of Aeronautics and Astronautics, National Cheng Kung University, Tainan 701, Taiwan, ROC

ARTICLE INFO

Article history:
Received 21 March 2009
Received in revised form 21 May 2009
Accepted 22 May 2009
Available online 30 May 2009

Keywords:
Hysteresis effect
Methane catalytic partial oxidation (CPO)
Syngas and hydrogen
Steam reforming
Rhodium
Numerical simulation

ABSTRACT

Hysteresis effects and reaction characteristics of methane catalytic partial oxidation (CPO) in a fixed-bed reactor are numerically simulated. The reactions are modeled based on the experimental measurements of methane CPO with a rhodium (Rh) catalyst. Three C/O ratios of 0.6, 1.0 and 1.4 are considered in the study. When the Reynolds number is 200, the predictions indicate that the methane CPO is always triggered at around the inlet temperature of 550 K, regardless of what the C/O ratio is. It is of interest that if the inlet temperature is decreased after the methane CPO develops at higher inlet temperatures, the reversed path of methane conversion is different from the original path at lower inlet temperatures. The hysteresis effect of the methane CPO is thus observed. The hysteresis behavior implies that a higher yield of syngas or hydrogen can be achieved by controlling the reaction process. Decreasing the C/O ratio intensifies the methane CPO so that the hysteresis effect is more pronounced, and vice versa. An increase in Reynolds number delays the excitation temperature of methane CPO and lessens the hysteresis effect of methane conversion due to the growth of fluid inertial force. However, the hysteresis effect of the maximum temperature in the catalyst bed increases as a result of more methane consumption.

© 2009 Elsevier B.V. All rights reserved.

1. Introduction

Methane is a common fuel which has been widely used for the purpose of getting heat, power and electricity. Methane is also an important raw material in the chemical industry. For example, from the steam reforming of methane, synthesis gas or syngas, a mixture of hydrogen and carbon monoxide, can be produced [1]. Syngas is commonly used for methanol and ethanol synthesis as well as Fisher–Tropsch process [2,3]. In recent years, because of the increasing interest in a more efficient and low pollution energy conversion system, there has been a pronounced progress in the development of fuel cells. Fuel cells can be operated in either low-, medium- or high-temperature environments, depending on the types of fuel cell [4]. For high-temperature fuel cells such as molten carbonate fuel cells (MCFCs) and solid oxide fuel cells (SOFCs), syngas can act as a feedstock to drive the devices and generate electricity [5]. Syngas can further be processed through water gas shift reactions [6,7] to promote the concentration of hydrogen. Once the hydrogen has been separated and purified, it can be used as a fuel in low- and medium-temperature fuel cells such as a proton exchange membrane fuel cell (PEMFC), an alkaline fuel cell (AFC) and a phosphoric acid fuel cell (PAFC).

Though steam methane reforming (SMR) is an important technique for producing syngas and hydrogen, the reaction pertains to a highly endothermic reaction in nature [8].

$$CH_4 + H_2O \leftrightarrow CO + 3H_2,\ \Delta H = +206\,kJ\,mol^{-1} \quad (1)$$

On account of the strong endothermic reaction of SMR, extra heat has to be supplied while the syngas is generated. To overcome this drawback, syngas or hydrogen generation from methane can be carried out by means of the method of catalytic partial oxidation (CPO) [9,10]. The process of methane CPO is

$$CH_4 + \tfrac{1}{2}O_2 \rightarrow CO + 2H_2,\quad \Delta H = 36\,kJ\,mol^{-1} \quad (2)$$

As a whole, the process is a mild exothermic reaction. In other words, instead of heat being supplied from a separate energy source, methane CPO is a naturally autothermal process. When the methane CPO is further analyzed, the detailed reactions include methane combustion, steam reforming and carbon dioxide reforming (or dry reforming) [8]. Specifically, the energy required for producing syngas is provided from the partial oxidation or combustion of methane. Methane combustion is a highly exothermic reaction and it is expressed as

$$CH_4 + 2O_2 \rightarrow CO_2 + 2H_2O,\ \Delta H = -803\,kJ\,mol^{-1} \quad (3)$$

* Corresponding author. Tel.: +886 6 2605031; fax: +886 6 2602205.
E-mail address: weihsinchen@gmail.com (W.-H. Chen).

0378-7753/$ – see front matter © 2009 Elsevier B.V. All rights reserved.
doi:10.1016/j.jpowsour.2009.05.042

Nomenclature

D_i	diffusion coefficient of species i ($m^2\ s^{-1}$)
D_p	mean particle diameter (m)
E	total energy (J)
E_a	activation energy (kJ mol^{-1})
F_i	mole fraction
h_i	enthalpy of species i (J kg^{-1})
h_i^0	standard-state enthalpy of species i (J kg^{-1})
ΔH°	change of total enthalpy on standard state
J_i	diffusion flux of species i (kg $m^{-2}\ s^{-1}$)
K_{eff}	effective thermal conductivity (W $m^{-1}\ K^{-1}$)
k_f	fluid phase thermal conductivity (W $m^{-1}\ K^{-1}$)
k_s	solid medium thermal conductivity (W $m^{-1}\ K^{-1}$)
k_{eq}	equilibrium constant
M_i	molecular weight of species i (kg $kgmol^{-1}$)
N	number of species
p	pressure (Pa)
r	radial coordinate (m)
R	universal gas constant (8.314 m^3 Pa K^{-1} mol^{-1})
R_i	reaction rate of species i (kmol $m^{-3}\ s^{-1}$)
S	selectivity
ΔS°	change of total entropy on standard state
T	temperature (K)
v	velocity (m s^{-1})
x	axial coordinate (m)
Y_i	mass fraction of species i

Greek letters

γ	porosity
ρ	density (kg m^{-3})
τ	shear stress (Pa)
μ	viscosity (Pa s)

Subscript

CH_4	methane
CO	carbon monoxide
com	combustion
cr	carbon dioxide reforming
f	fluid
H_2O	water
i	species i
in	inlet
N_2	nitrogen
out	outlet
sr	steam reforming
steam	steam
w	wall

With the aid of catalysts, syngas formation from methane can be triggered at a lower temperature environment and the heat released from the combustion is able to induce the subsequently endothermic reactions of steam reforming (i.e. Eq. (1)) and carbon dioxide reforming. The reaction of carbon dioxide reforming is written as the following

$$CH_4 + CO_2 \leftrightarrow 2CO + 2H_2,\ \Delta H = 247\ kJ\ mol^{-1} \quad (4)$$

Accordingly, it is known that the products of methane combustion (i.e. H_2O and CO_2) are then reduced to hydrogen and carbon monoxide, thereby yielding syngas.

It is known that catalysts, which are used in methane CPO, play a key role in determining the methane conversion and syngas formation. In this aspect, some group VIII or noble metals such as Ni, Pt, Ru and Rh have been widely employed and they are usually supported on certain oxides such as α-Al_2O_3 and RuO_2. For instance, in the earlier of study of Prettre et al. [11], methane CPO was conducted over 10 wt% refractory supported nickel in the temperature range of 973–1173 K at 1 atm. Ashcroft et al. [12] studied methane CPO with the catalysts of lanthanide ruthenium oxides as well as Ru supported on Al_2O_3 and pure RuO_2 at 1050 K and 1 atm. They reported that methane conversion was in excess of 90% and syngas selectivity was in the range of 94–99%. In the experimental study of Horn et al. [13], methane CPO on Rh and Pt foam catalysts were analyzed and compared with each other. They reported that Rh catalyzed steam reforming much more efficiently than Pt so that the hydrogen and carbon monoxide yields were generally higher on the former than on the latter.

In addition to experimental studies, a number of numerical simulations have also been performed to figure out the detailed reaction processes of methane CPO. In the earlier studies of Hickman and Schmidt [14,15], methane CPO over Pt and Rh surfaces were predicted using a model which consisted of 19 elementary steps including adsorption, desorption and surface reactions. It was illustrated that, under methane-rich conditions at high-temperatures, H_2 and CO were the primary products of methane direct oxidation through a pyrolysis mechanism. Potential energy diagrams were also displayed in their studies. The study of Williams et al. [16] further developed two different mechanisms to predict methane CPO on Rh-coated foam monoliths; one was a 38-step mechanism and the other a 104-step mechanism. They highlighted the importance of high-resolution spatial profiles for each mechanism. Unlike the aforementioned multi-step mechanisms developed, Jin et al. [17] modeled and simulated methane CPO in a membrane reactor using one-step global chemical mechanisms. In spite of such simple kinetics, their simulated results were in good agreement with the experimental data and it was found that at a low carbon space velocity and when the temperature was between 1098 and 1158 K, CH_4 conversion was larger than 96% and CO selectivity was larger than 97%. Abashar et al. [18] used the developed model of Jin et al. [17] to predict the coupled steam and oxidative reforming reactions of methane in a circulating, fast fluidized bed membrane reactor where an oxygen discrete injection was proposed to overcome the hot spot temperature problem.

The above literature has provided some important information to describe the reaction characteristics of methane CPO and these studies are conducive to practicing the production of syngas and hydrogen for industrial purposes. As illustrated above, Rh catalysts are usually more appropriate than Pt catalysts for syngas generation [13]. As a result, the present study is intended to establish reaction models in terms of a number of one-step global chemical mechanisms to describe methane CPO on Rh. Particular emphasis is placed on the hysteresis effects of methane CPO at various inlet conditions. Details of the hysteresis effect and reaction behavior of the methane CPO on Rh will be pointed out.

2. Mathematical formulation and modeling

2.1. Geometry and assumptions

A schematic of the computational geometry and physical size of the studied fixed-bed reactor is sketched in Fig. 1a where the simulation is performed in a cylindrical tube. The geometry of the reactor is constructed based on the experimental set-up of Horn et al. [13]. As a whole, the reactor consists of three zones. The middle (second) zone is filled with the Rh catalyst which is sandwiched by the first and third zones. The first and third zones remain empty for fluid to flow inward and outward from the catalyst bed, respectively. These three zones are enveloped by a cylindrical shell with an adiabatic wall. Therefore, the released heat will not penetrate through the tube wall.

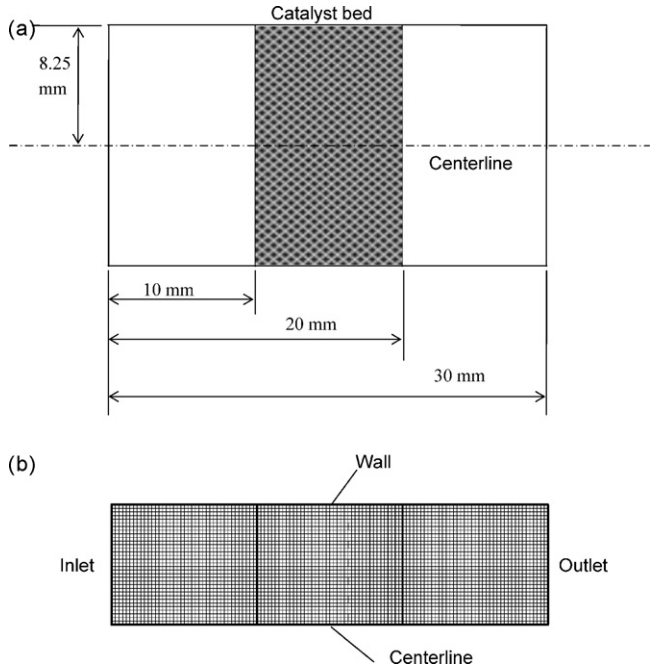

Fig. 1. Schematics of (a) computational geometry and reactor size as well as (b) adopted grid system (120 × 33).

Seeing that the investigated phenomena are related to fluid motion, heat and mass transfers as well as chemical reactions, some assumptions are adopted to simplify the physical problem. They include: (1) the flow field is laminar and axisymmetric along the centerline of the reactor, whereby the two-dimensional simulation is carried out; (2) the porous media in the catalyst bed is homogeneous and thermal equilibrium prevails at the catalyst surface so that there is no temperature difference at the interface of the catalyst and the fluid [4,13]; (3) the effect of gravity on the flow field and the reactions of reagents are ignored; and (4) gas mixture inside the reactor abides by the ideal gas law.

2.2. Governing equations

By virtue of the chemical reactions inside a catalyst bed encountered, two kinds of governing equations are considered to take the non-porous and porous zones into account. In the non-porous regions, the governing equations include

Continuity equation:

$$\nabla \cdot (\rho \vec{v}) = 0 \tag{5}$$

Momentum equation:

$$\nabla \cdot (\rho \vec{v}\vec{v}) = -\nabla p + \nabla \cdot \left(\vec{\tau}\right) \tag{6}$$

Energy equation:

$$\nabla \cdot (\vec{v}(\rho E + p)) = \nabla \cdot [k \nabla T - (\sum_i h_i J_i) + (\bar{\bar{\tau}} \cdot \vec{v})] \tag{7}$$

In the porous region or the catalyst bed, the governing equations contain

Continuity equation:

$$\nabla \cdot (\gamma \rho \vec{v}) = 0 \tag{8}$$

Momentum equation:

$$\nabla \cdot (\gamma \rho \vec{v}\vec{v}) = -\gamma \nabla p + \nabla \cdot \left(\gamma \vec{\tau}\right) - \frac{150 \cdot \mu}{D_p^2} \frac{(1-\gamma)^2}{\gamma^3} v_\infty \tag{9}$$

Energy equation:

$$\nabla \cdot (\vec{v}(\rho_f E_f + p)) = \nabla \cdot [k_{eff} \nabla T - (\sum_i h J_i) + (\bar{\bar{\tau}} \cdot \vec{v})] - \sum_i^N \frac{h_i^0}{M_i} R_i \tag{10}$$

where $K_{eff} = \gamma k_f + (1-\gamma) K_s$. In both the non-porous and porous regions, the species equation and the equation of state are also invoked. They are given as follows.

Species equation:

$$\nabla \cdot (\rho \vec{v} Y_i) = \nabla \cdot (\rho D_i \nabla Y_i) + M_i \sum_{i=1}^{N} R_i \tag{11}$$

Equation of state:

$$p = \rho R T \sum_i^N \frac{Y_i}{M_i} \tag{12}$$

2.3. Boundary conditions

When boundary conditions are considered, four different sections are involved, including the upstream inflow, the downstream outflow, the centerline and the wall. For the upstream inflow, the boundary conditions are given by

$$u = u_{in}, v = v_{in}, Y_i = Y_{i,in}, T = T_{in}, \text{ and } p = p_{in} \tag{13}$$

In regard to the downstream outflow, they are

$$\nabla \cdot \vec{v} = \nabla Y_i = \nabla T = 0 \tag{14}$$

By virtue of the absence of heat and mass fluxes across the centerline, the boundary conditions along the axissymmetric axis can be treated as the following

$$v = \frac{\partial u}{\partial r} = \frac{\partial T}{\partial r} = \frac{\partial Y_i}{\partial r} = 0 \tag{15}$$

Inside the reactor surface, the no-slip velocity and adiabatic wall are encountered. Hence, the boundary conditions are expressed to be

$$u = v = \frac{\partial Y_i}{\partial r} = \frac{\partial T}{\partial r} 0 \tag{16}$$

2.4. Model of methane CPO

As far as the chemical reactions are concerned, it is known that accurate predictions of physical phenomena are highly related to reaction rate expressions and the chemical reaction rates depend strongly on the catalyst employed. Presently, numerical simulations of methane CPO on an Rh catalyst are performed. Similar to the one-step global chemical mechanisms adopted by Jin et al. [17] and Abashar et al. [18], the reaction rates of methane combustion (R_{com}), steam reforming (R_{sr}) and carbon dioxide reforming (R_{cr}) are also modeled using one-step global chemical mechanisms. However, the rate expressions are established based on the experimental data of Horn et al. [13] and they are given in the following forms

$$R_{com} = 2.119 \times 10^{10} \exp\left(\frac{-80}{RT}\right) p_{CH_4} p_{O_2} \tag{17}$$

$$R_{sr} = 1.0 \times 10^{-9} T^5 \exp\left(-\frac{47.3}{RT}\right) \left(p_{CH_4} p_{H_2O} - K_{eq,sr}^{-1} p_{CH_4} p_{H_2O}\right) \tag{18}$$

$$R_{cr} = 7.0 \times 10^{-7} T^4 \exp\left(-\frac{32.0}{RT}\right) \left(p_{CH_4} p_{CO_2} - K_{eq,cr}^{-1} p_{CH_4} p_{CO_2}\right) \tag{19}$$

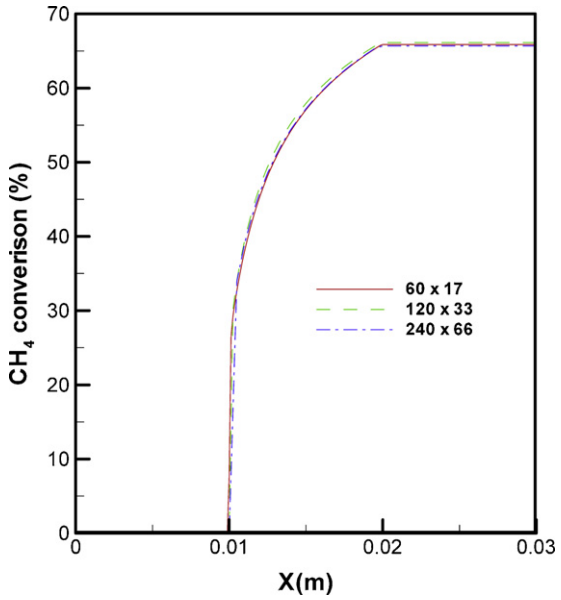

Fig. 2. Distributions of methane conversion along the centerline of the catalyst bed at three different grid systems.

where K_{eq} is the equilibrium constant which links the forward and backward reactions. The constant is obtained in accordance with the thermodynamic theory [19] and it is expressed as

$$K_{eq} = \exp\left(\frac{\Delta S^{\circ}}{R} - \frac{\Delta H^{\circ}}{RT}\right) \quad (20)$$

2.5. Numerical method

To predict the methane CPO phenomena in association with the aforementioned models, the commercial software FLUENT (Version 6.2) is utilized to solve the governing equations along with the boundary conditions. In brief, the finite-volume method in association with SIMPLE algorithm [20] is utilized. The first order upwind scheme is used to evaluate the convective and diffusive fluxes over the control volume surface. An orthogonal grid system is employed to reduce numerical truncation errors, which may occur during the course of calculating. Regarding the grid system, the grids are uniformly distributed along the *x*- and *y*-axes. Three different grid systems of 60 × 17, 120 × 33 and 240 × 66 are tested and compared with each other to seek a proper grid system for simulations. With the three grid systems, the distributions of methane conversion along the centerline of the reactor in the catalyst bed are shown in Fig. 2 where the inlet temperature is 300 °C and the C/O ratio is 1. It is obvious that no matter which grid system is adopted, the discrepancy among the three curves is almost imperceptible. In view of the grid system of 120 × 33 satisfying the requirement of grid independence, it is employed to simulate the phenomena of methane CPO.

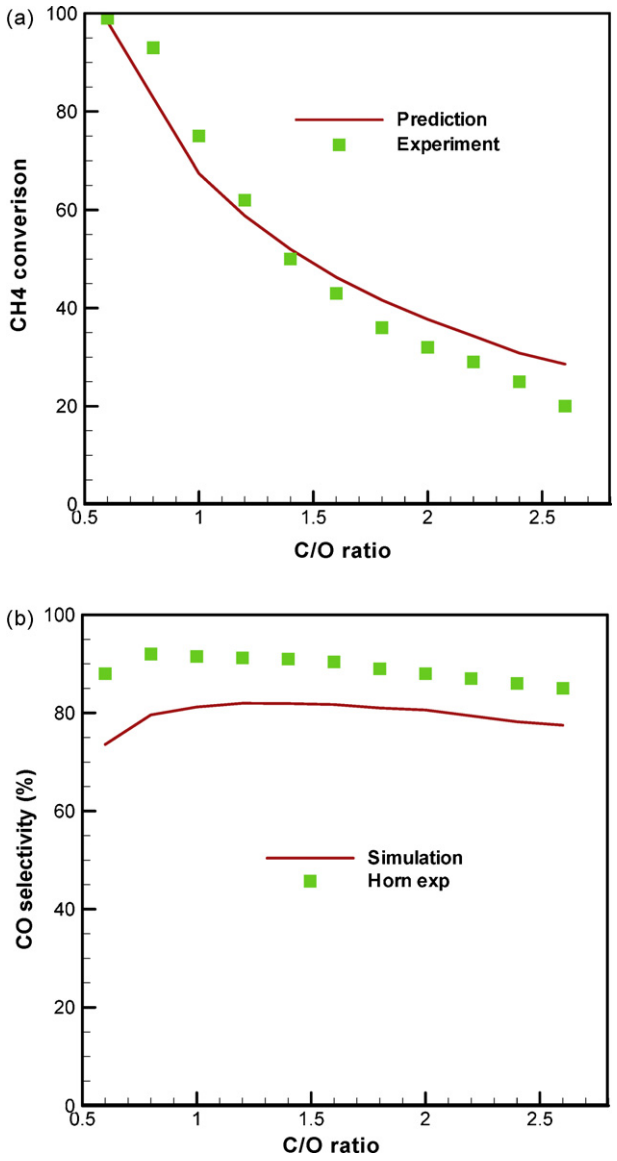

Fig. 3. Comparisons of (a) methane conversion and (b) CO selectivity between the numerical simulation and the experimental measurement.

To validate the developed models and adopted numerical methods, comparisons between the numerical predictions and the experimental measurements [13] are displayed in Fig. 3 where the methane conversion and CO selectivity at the exit of the reactor are plotted. In the experiments of Horn et al. [13], methane mixed with oxygen and argon passing through the Rh catalyst bed was carried out. As a whole, the numerical predictions of the methane conversion are in agreement with the experimental data (Fig. 3a).

Table 1
Inlet conditions of methane CPO and the properties of the catalyst.

Feed (based on 300 K) Feed flow rate ($m^3\ s^{-1}$)	Re	GHSV (h^{-1})	Feed composition (mol%)	C/O = 0.6	C/O = 1.0	C/O = 1.4
8.91×10^{-5}	200	185,240	CH_4	20.13	29.60	37.03
			O_2	16.77	14.80	13.22
			N_2	63.10	55.60	49.75

Properties of the catalyst

Composition (wt%)	Porosity of catalyst bed	Bulk density ($kg\ m^{-3}$)	Specific heat ($J\ kg^{-1}\ K^{-1}$)	Thermal conductivity ($W\ m^{-1}\ K^{-1}$)
5% Rh + 95% α-Al_2O_3	0.81	4325	848	36

The predicted results of CO selectivity are somewhat lower than the experimental measurements (Fig. 3b). Nevertheless, the trend of the former is consistent with the latter. As a consequence, Fig. 3 depicts that the established models and adopted numerical method enable us to investigate the phenomena of methane CPO on the Rh catalyst appropriately.

3. Results and discussion

Methane mixed with air flowing through the Rh catalyst bed serves as the basis for the present study. The stream in the tube is at atmospheric pressure and the Reynolds number is fixed at 200. Accordingly, the volumetric flow rate of the gaseous mixture at the inlet is 8.91×10^{-5} m^3 s^{-1} and the gas hourly space velocity (GHSV) is around 185,240 h^{-1}, based on the temperature of 300 K. Three different C/O ratios are considered; they are 0.6, 1.0 and 1.4. Detailed operational conditions and the properties of the catalyst are listed in Table 1.

3.1. Hysteresis effect of methane CPO

Methane conversion and the maximum temperature in the reactor versus inlet temperature, where the inlet temperature ranges from 300 to 800 K and the C/O ratio is 1, are sketched in Fig. 4a and b, respectively. The methane conversion (x_{CH_4}) is defined to be:

$$x_{CH_4}(\%) = \frac{F_{CH_4,in} - F_{CH_4,out}}{F_{CH_4,in}} \times 100\% \quad (21)$$

When the inlet temperature proceeds from 300 to 500 K, the methane conversion is zero (Fig. 4a). This indicates that no chemical reaction is triggered, whereby the chemical-frozen flow is exhibited. Once the inlet temperature is increased to 550 K, methane CPO is triggered so that there is a pronounced jump in

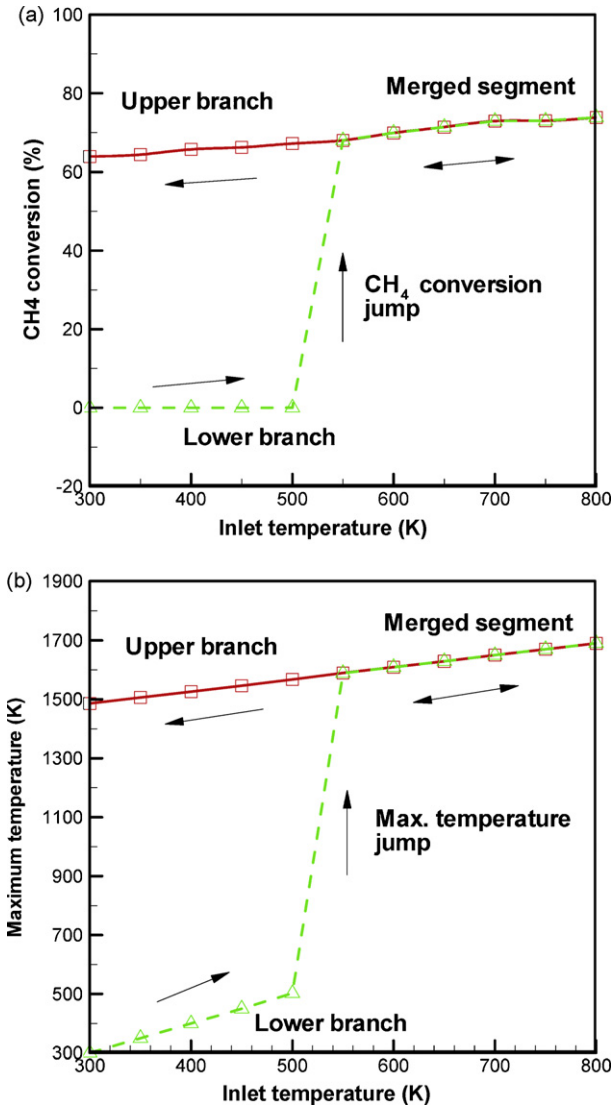

Fig. 4. Distributions of (a) methane conversion and (b) the maximum temperature versus inlet temperature in the upper branch and the lower branch at the exit.

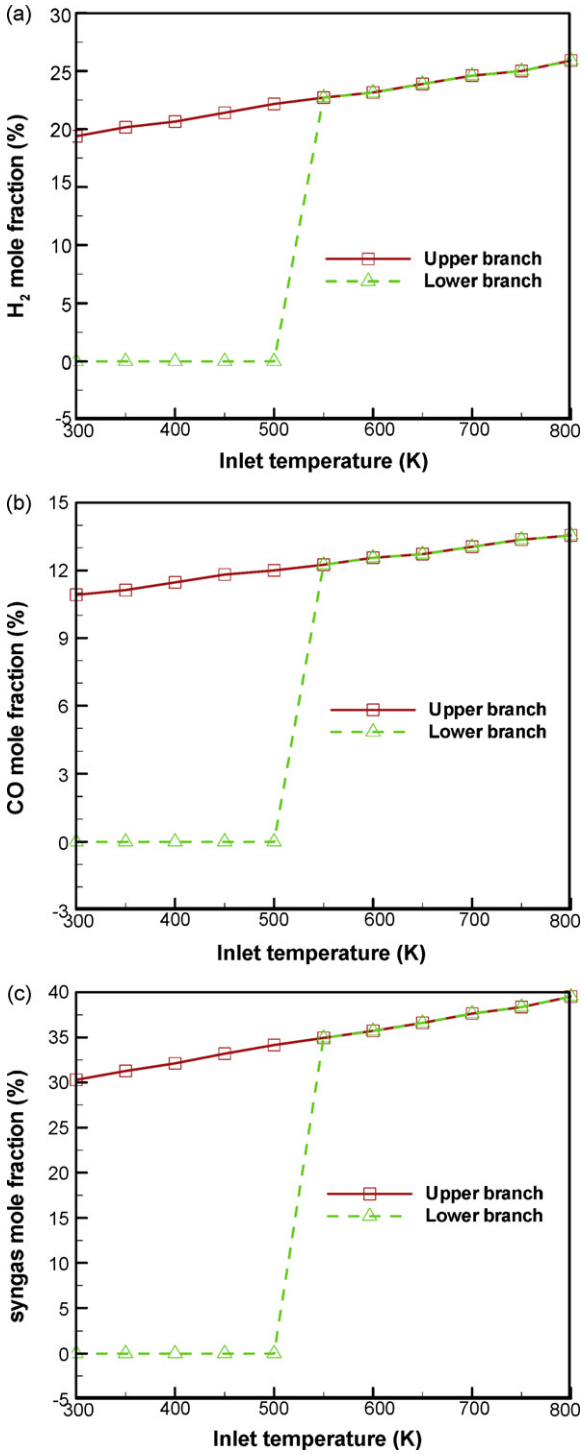

Fig. 5. Concentration distributions of (a) H_2, (b) CO and (c) syngas versus inlet temperature in the upper branch and the lower branch at the exit.

methane conversion. Specifically, the methane conversion rises from 0 to 69% (Fig. 4a). On the other hand, by virtue of the partial combustion or violent oxidation of methane induced, heat is liberated from the exothermic reaction which results in a sudden growth in the maximum temperature (Fig. 4b). At the inlet temperature (550 K), the maximum temperature is around 1590 K. However, this temperature is relatively low compared to the adiabatic flame temperature of methane. Typically, the constant-pressure adiabatic flame temperature for the combustion of a stoichiometric methane–air mixture is 2318 K [21]. The lower maximum temperature is attributed to the fact that only part of the methane is depleted for combustion, as observed in Fig. 4a. Normally, the ignition temperature of methane is 905 K [22] which is much higher than the activated temperature of the methane CPO (550 K). This indicates that the role, played by the Rh catalyst on the methane CPO, is of the utmost importance. After the methane CPO is excited, both the methane conversion and the maximum temperature increase slightly with the increasing inlet temperature.

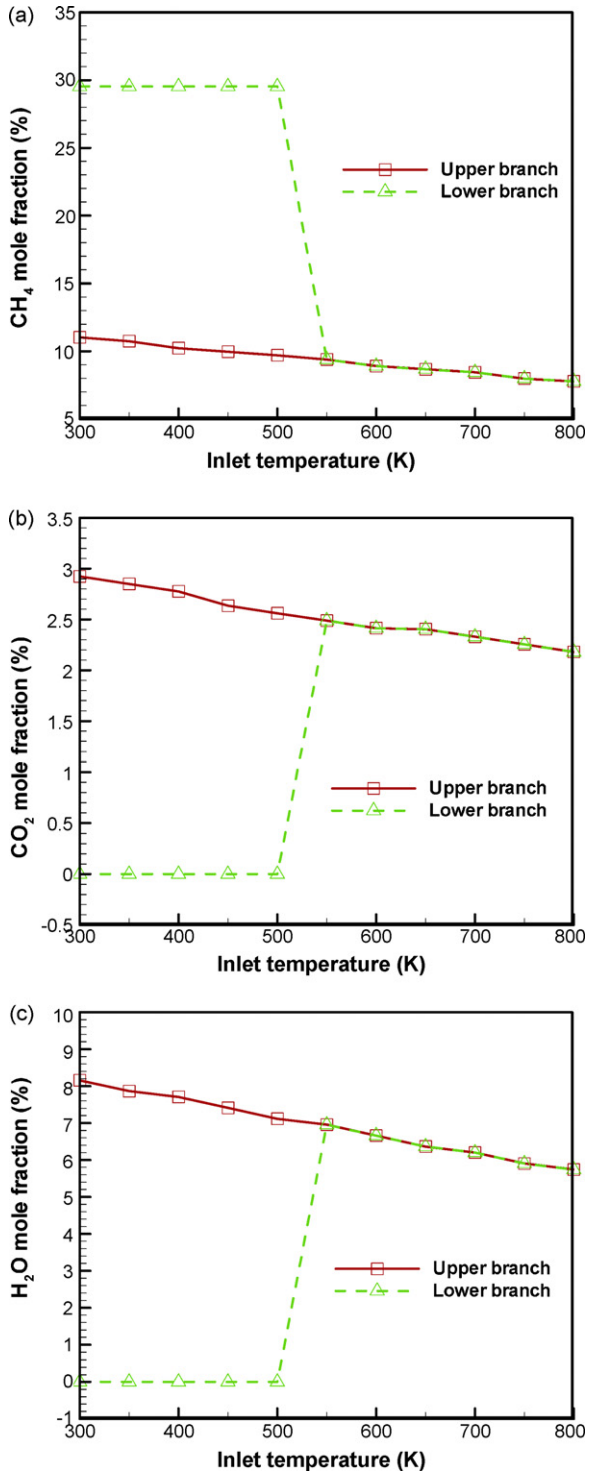

Fig. 6. Concentration distributions of (a) CH_4, (b) CO_2 and (c) H_2O versus inlet temperature in the upper branch and the lower branch at the exit.

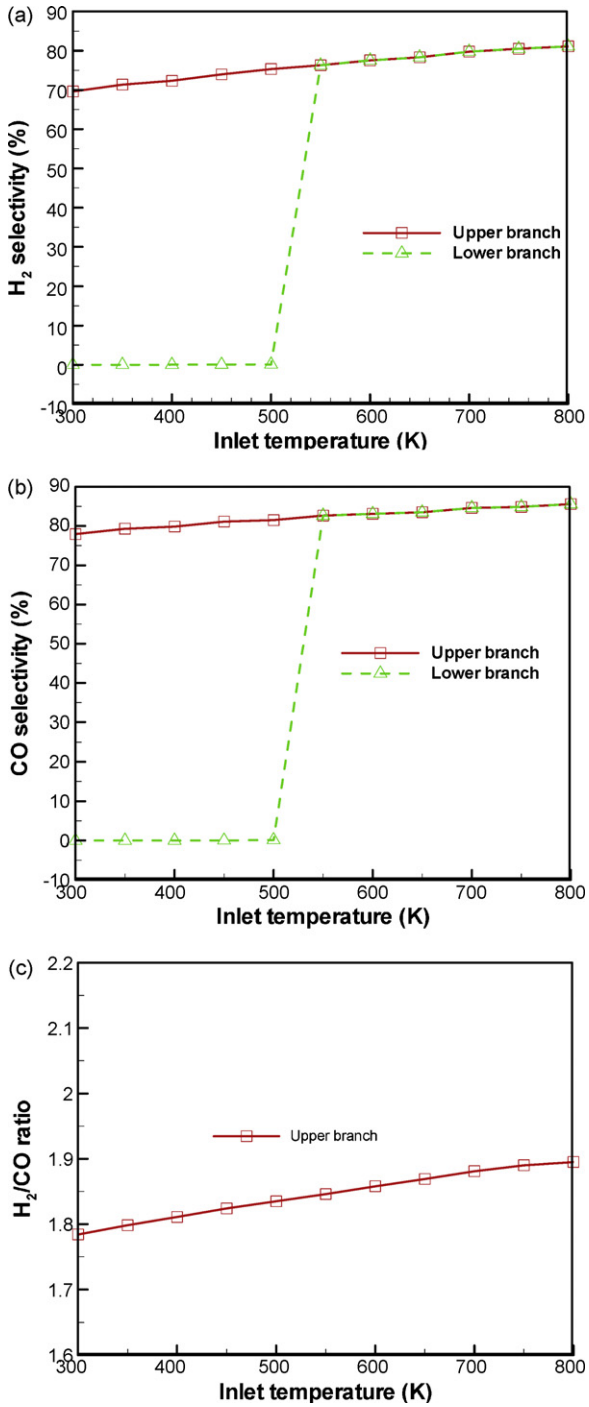

Fig. 7. Distributions of (a) H_2 selectivity, (b) CO selectivity and (c) H_2/CO versus inlet temperature in the upper branch and the lower branch at the exit.

If the inlet temperature goes down from 800 K, the backward paths (the upper branch solutions) of both the methane conversion and the maximum temperature are equivalent to the forward paths (the lower branch solutions). The merged segment lasts until the excitation temperature of methane CPO (i.e. 550 K). Once the inlet temperature is lower than 550 K, it is of interest that the methane conversion and the maximum temperature decline only a bit with the decreasing inlet temperature, even though the inlet temperature goes as low as 300 K. In other words, the reversed paths are totally different from the original paths as the inlet temperature is lower than 550 K. Physically, as long as the methane CPO has been triggered, the cooling effect brought by the inlet stream is insufficient to eliminate the heat released from the CPO. As a result, the chemical reaction sustains itself. It is thus recognized that the methane CPO with respect to inlet temperature is characterized by a hysteresis effect. Alternatively, for the presently studied conditions (i.e. C/O = 1 and Re = 200), the upper branch and the lower branch are separated at the excitation point of methane CPO. It follows that the bifurcation point of the dual-solution exactly stands for the activated temperature of methane CPO in the lower branch. Reviewing the past studies concerning fuel burning, hysteresis effects have been observed in single-droplet combustion [23,24], two-droplet combustion [25,26], lifted flame [27] and swirling flame [28] systems. Obviously, even though the methane reaction in a CPO system is not as strong as those of the aforementioned burning systems, the hysteresis effect is still featured due to the partial combustion of methane.

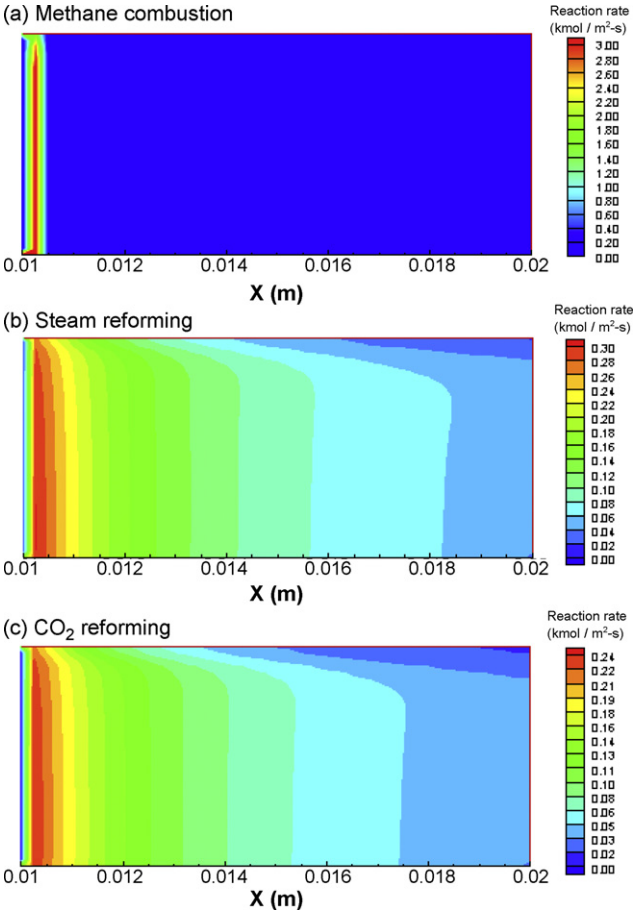

Fig. 8. Upper-branching reaction rate contours of (a) methane combustion, (b) steam reforming and (c) carbon dioxide reforming in the catalyst bed with the inlet temperature of 300 K.

3.2. Performance of methane CPO

Subsequently, the exit concentration (or mole fraction) distributions of H_2, CO and syngas (i.e. H_2 + CO) versus inlet temperature in the upper branch and the lower branch are presented in Fig. 5 to figure out the performance of the methane CPO. When the inlet temperature is lower than 550 K, no reaction develops so that the concentrations of H_2, CO and syngas are zero. After the two branches merge, increasing inlet temperature makes these concentrations rise a bit. The methane CPO is a slightly exothermic reaction, as expressed in Eq. (2). Basically, it is composed of a forward combustion reaction and two reversible reforming reactions. It should be emphasized that the formation of H_2 and CO comes from H_2O and CO_2 reforming (i.e. Eqs. (1 and 4)). The two reactions pertain to an endothermic reaction where a higher reaction temperature is conducive to the production of syngas. Besides, the generation of H_2O and CO_2 is subject to the methane combustion (i.e. Eq. (3)). In other words, a higher inlet temperature facilitates the formation of H_2O and CO_2 in the methane combustion reaction and, furthermore, the steam and dry reforming reactions shift toward the formation of H_2 and CO. This results in the enhancement in the concentrations of H_2, CO and syngas when the inlet temperature increases. The concentration distributions of CH_4, H_2O and CO_2 in the upper branch and the lower branch are provided in Fig. 6. Apparently, the concentration of CH_4 falls when the methane CPO is excited in the lower branch. On the other hand, unlike the distributions shown in Fig. 5, the concentrations of CH_4, H_2O and CO_2 decline in the upper branch as the inlet temperature increases, verifying that increasing inlet temperature enhances the forward reactions of H_2O and CO_2 reforming.

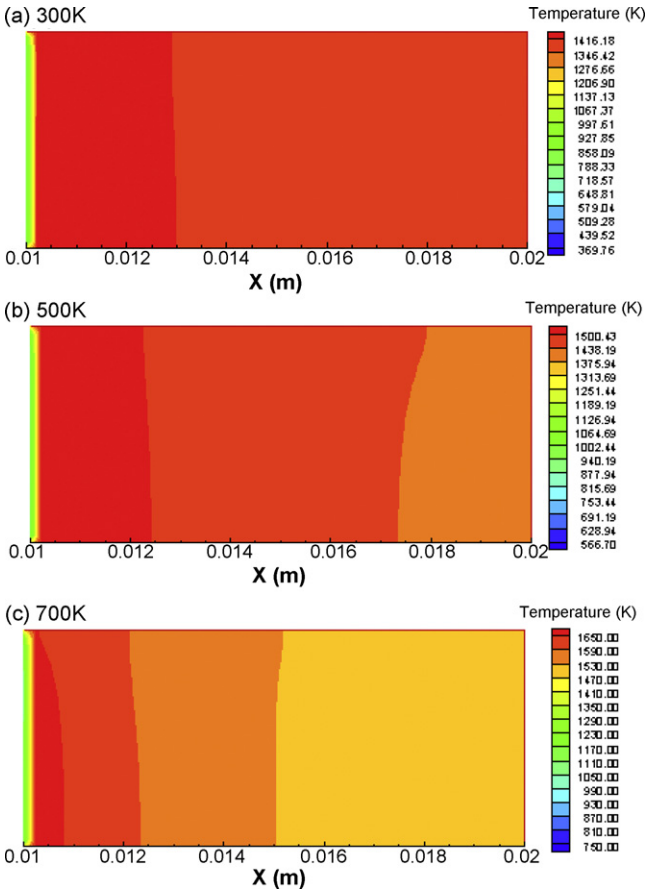

Fig. 9. Upper-branching isothermal contours in the catalyst bed with the inlet temperatures of (a) 300 K, (b) 500 K, and (c) 700 K.

The profiles of H_2 and CO selectivity in the two branches as well as H_2/CO ratio (mole fraction ratio) in the upper branch are plotted in Fig. 7. The H_2 selectivity (S_{H_2}) and CO selectivity (S_{co}) are defined as:

$$S_{H_2} = \frac{F_{H_2,out}}{F_{H_2,out} + F_{H_2O,out}} \times 100\% \quad (22)$$

$$S_{CO} = \frac{F_{CO,out}}{F_{CO,out} + F_{CO_2,out}} \times 100\% \quad (23)$$

It is known that, following the conversion of methane, both H_2 and H_2O are generated when one is concerned with hydrogen elements. The higher the H_2 selectivity, more H_2O is converted into H_2. Within the investigated range of the inlet temperature (300–800 K), the H_2 selectivity is always higher than 70% (Fig. 7a), revealing that H_2 rather than H_2O is the main product. It has been noted in Fig. 5 that a higher inlet temperature gives a higher maximum temperature, which is conducive to the forward reaction of H_2O reforming from the viewpoint of Le Chatelier's principle. This is the reason that the H_2 selectivity rises with increasing inlet temperature. The CO selectivity also grows with increasing inlet temperature and the value is larger than 77% (Fig. 7b), reflecting that CO formation dominates the competition between CO and CO_2 generations. In examining Eq. (2), it is known that the concentration ratio between H_2 and CO from an ideal reaction of methane partial oxidation should be 2. Observing the curve shown in Fig. 7c, an ascent in inlet temperature is closer to the theoretical result.

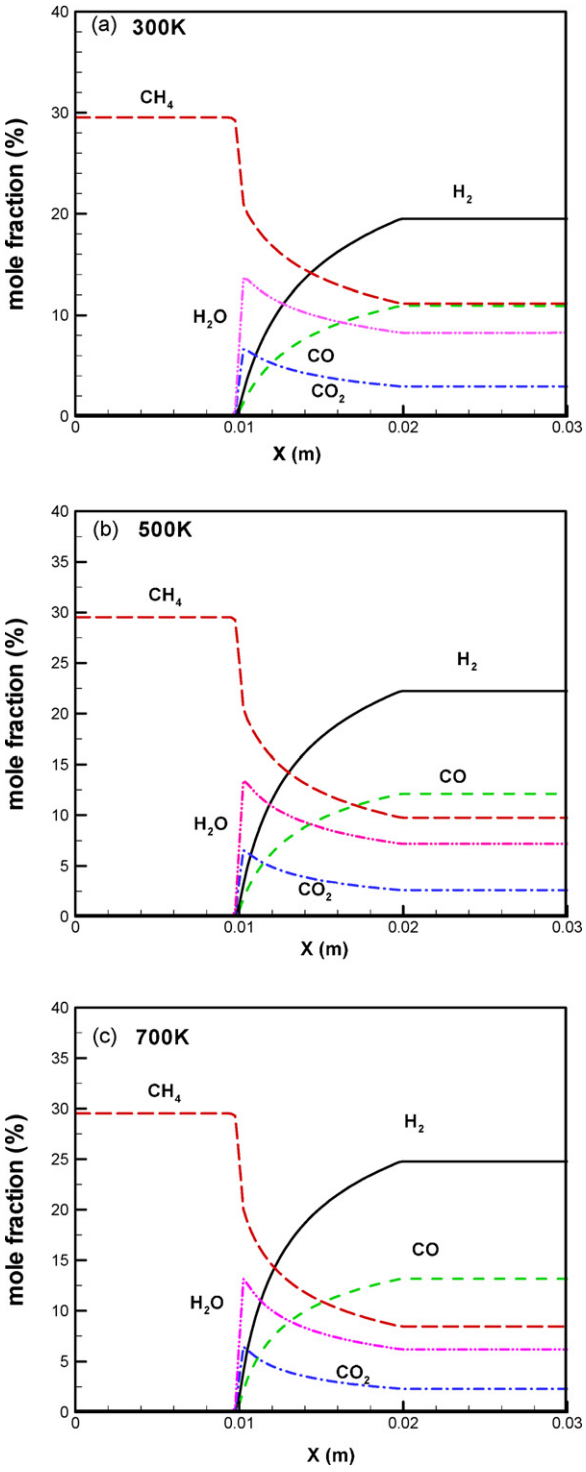

Fig. 10. Concentration distributions of H_2, CO, CO_2, CH_4 and H_2O along the centerline of the reactor in the upper branch with the inlet temperatures of (a) 300 K, (b) 500 K, and (c) 700 K.

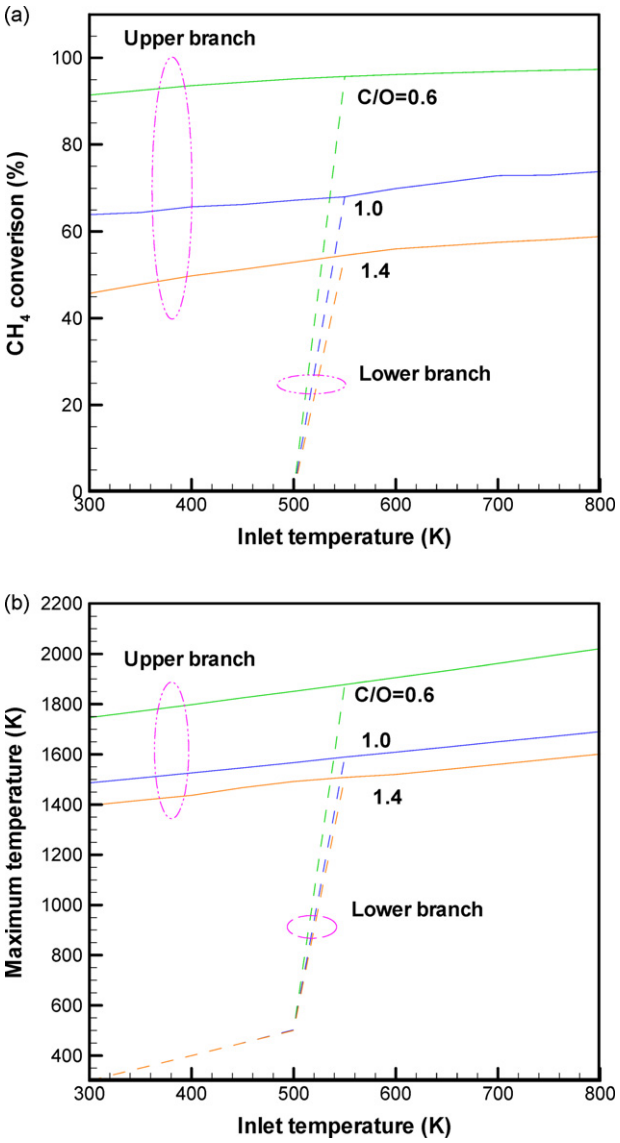

Fig. 11. Distributions of (a) methane conversion and (b) the maximum temperature versus inlet temperature in the upper and lower branch at various C/O ratios.

3.3. Reaction characteristic of methane CPO

To proceed farther into an analysis of methane CPO, the reaction contours of methane combustion, steam reforming and dry reforming in the catalyst bed with the upper branch solution at 300 K are displayed in Fig. 8. Soon after the reactants flow into the catalyst bed, methane combustion occurs within a very thin layer, behaving as a flame sheet (Fig. 8a). In contrast, the steam reforming and CO_2 reforming prevail over the entire catalyst bed. When observing the reaction rate expressions in Eqs. (17–19), the activation energy of methane combustion is much higher than those of steam and carbon dioxide reforming. It is thus realized that all the reactions are controlled by the combustion. Moreover, on account of inherently endothermic reactions featured by the steam reforming and dry reforming, only after the combustion is triggered, the steam and carbon dioxide reforming can proceed by means of the liberated heat.

Fig. 9 shows the upper-branching isothermal contours inside the catalyst bed at the inlet temperatures of 300, 500 and 700 K. Though a lower inlet temperature (300 K) causes a lower bed temperature (Fig. 10a) and vice versa (Fig. 10c), the temperature variation is not very significant. Fig. 10 further plots the concentration profiles of H_2, CO, CO_2, CH_4 and H_2O along the centerline of the reactor at the three inlet temperatures. A rapid drop in CH_4 concentration is observed in the vicinity of the entrance of the catalyst bed, whereas the concentration distributions of H_2O and CO_2 are characterized by a peak at a certain location, as a consequence of methane combustion. Alternatively, a progressive growth in the concentrations of H_2 and CO is obtained. As a whole, the higher the inlet temperature, the more pronounced the concentration difference between CO and CO_2 as well as H_2 and H_2O.

3.4. Effects of C/O ratio and Reynolds number on hysteresis behavior

The distributions of methane conversion and the maximum temperature in the catalyst bed at various C/O ratios (i.e. 0.6, 1.0 and 1.4) are evaluated in Fig. 11, whereas the distributions of CO and H_2 selectivity are displayed in Fig. 12. As seen in Fig. 11a, within the investigated range of C/O ratio, the activated temperature of methane CPO is hardly affected by the ratio. Once the inlet tem-

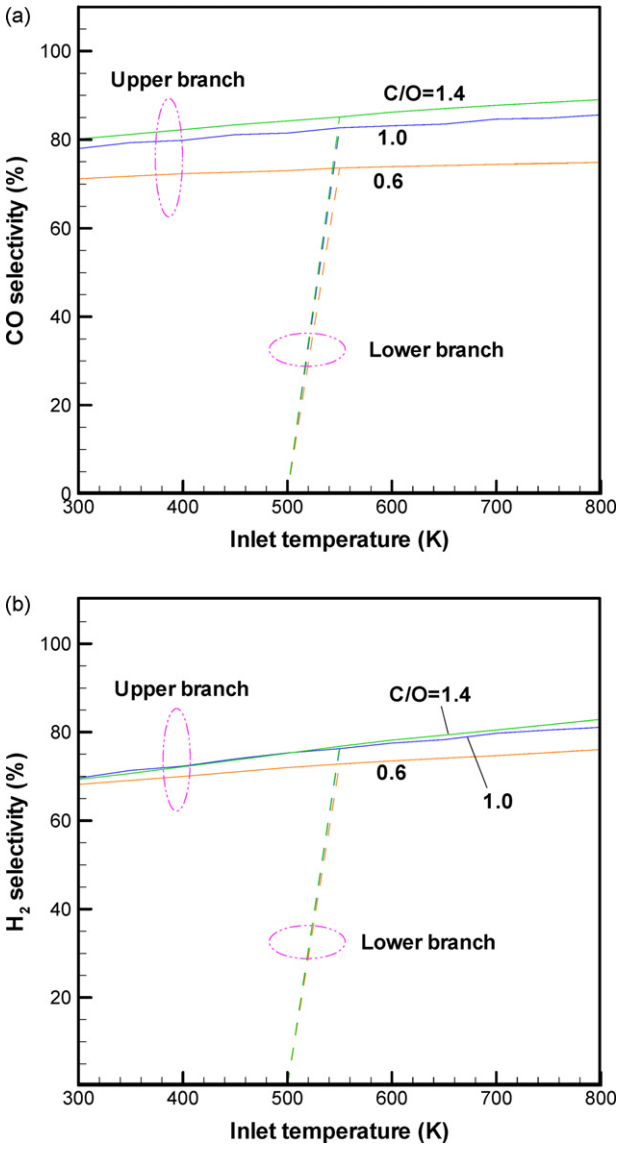

Fig. 12. Distributions of (a) CO selectivity and (b) H_2 selectivity versus inlet temperature in the upper and lower branch at various C/O ratios.

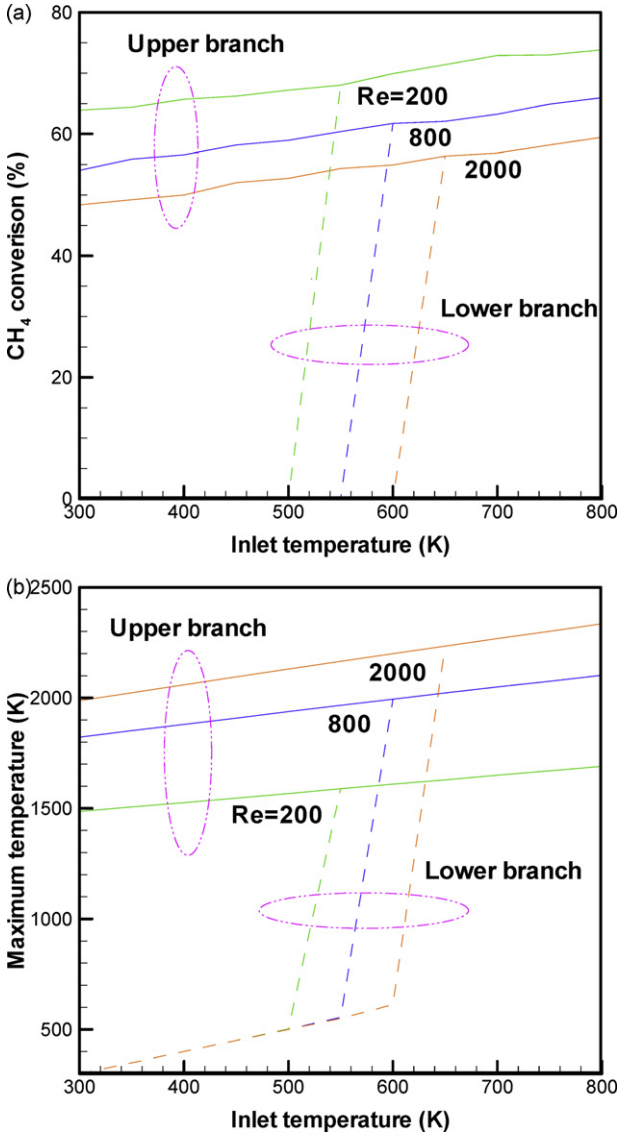

Fig. 13. Distributions of (a) methane conversion and (b) the maximum temperature versus inlet temperature in the upper and lower branch at various Reynolds numbers.

perature is high enough to induce the methane CPO, the methane conversion with C/O = 0.6 is much higher than that with C/O = 1.0 and 1.4, resulting from the richer oxygen contained in the stream. As a consequence, the hysteresis effect of the methane CPO at C/O = 0.6 is more profound. Since the methane CPO at C/O = 0.6 is closer to the complete combustion of methane, it is not surprising that the maximum temperature of the reaction is promoted, in contrast to that of C/O = 1.0 and 1.4 (Fig. 11b). Conversely, from the distributions of CO and H_2 selectivity shown in Fig. 12, increasing C/O ratio is conducive to the formation of CO and H_2, whereby the concentration of syngas in the product gas rises.

The effect of varied Reynolds number on the hysteresis phenomena are examined in Figs. 13 and 14 where three different Reynolds numbers of 200, 800 and 2000 are considered. As the Reynolds number increases, the inertial force of the inlet stream increases and the residence time for the reactants in the catalyst bed decreases. As a result, the methane CPO develops at a higher inlet temperature and the hysteresis behavior is less notable when the Reynolds number is larger (Fig. 13a). Nevertheless, it is worthy of note that the hysteresis effect of the maximum temperature increases rather than decreases with increasing the Reynolds number (Fig. 13b). This arises from the fact that more reactants are fed into the catalyst bed and thereby more heat is liberated from methane combustion, even though the methane conversion is reduced. Owing to the lower methane conversion at higher Reynolds numbers, the methane CPO tends to reduce the formation of CO and H_2, as observed in Fig. 14.

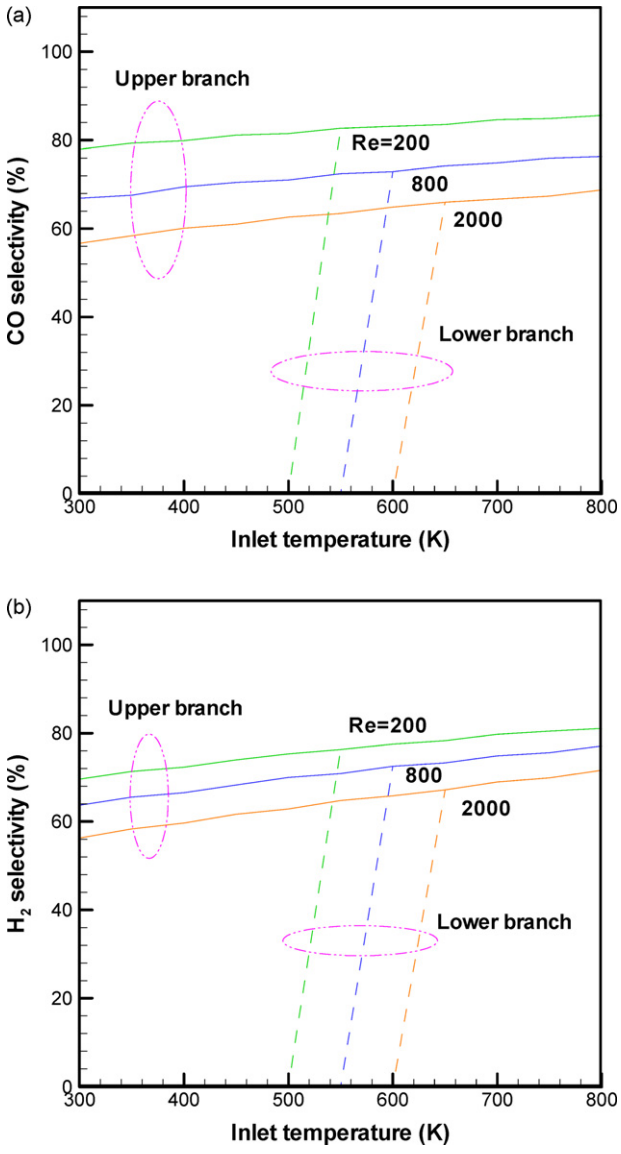

Fig. 14. Distributions of (a) CO selectivity and (b) H_2 selectivity versus inlet temperature in the upper and lower branch at various Reynolds numbers.

4. Conclusions

The chemical kinetics simultaneously considering methane combustion, steam reforming and carbon dioxide reforming has been successfully modeled to account for the reaction characteristics of methane catalytic partial oxidation on a Rh catalyst. When the Reynolds number is fixed (i.e. Re = 200), the methane CPO is activated at around 550 K and this excited temperature is hardly affected by the C/O ratio. With increasing the inlet temperature to the activated temperature followed by decreasing the inlet temperature, it is worthy of note that different paths of the CH_4 conversion and the maximum temperature are exhibited, yielding a hysteresis effect. The hysteresis effect developed is mainly due to the exothermic reaction of methane combustion. It follows that the historical trajectory of energy state in the catalyst bed plays a vital role in determining the result of methane CPO. When the inlet temperature is 300 K and C/O = 1, the values of the CH_4 conversion in the upper and lower branches are 64 and 0%, respectively. Therefore, from the viewpoint of methane CPO operation, the upper branch is a better condition for generating syngas and hydrogen. The reaction contours indicate that methane combustion behaves as a flame sheet, which takes place in the vicinity of the reactor entrance, whereas steam reforming and dry reforming prevail over the entire catalyst bed. It is thus recognized that the methane CPO is controlled by the combustion reaction. As a whole, an increase in inlet temperature facilitates the formation of H_2 and CO. This arises from the fact that increasing inlet temperature enhances the methane combustion and thereby increases the formation of H_2O and CO_2. The increased H_2O and CO_2 further facilitate the generation of syngas, resulting from the endothermic reactions of steam reforming and carbon dioxide reforming. Decreasing C/O ratio renders the reaction to approach complete combustion from partial oxidation; as a result, the hysteresis effect becomes more significant. Alternatively, the hysteresis effect withers if the C/O ratio goes up. On the other hand, increasing the Reynolds number results in the decline of the hysteresis effect due to the enhancement of the inertial force of the inlet stream. However, more methane is depleted and more heat is released as the Reynolds number increases, the hysteresis behavior of maximum temperature is thus enlarged, despite the lower methane conversion.

Acknowledgements

The authors gratefully acknowledge the financial supported of the National Science Council, Taiwan, ROC, on this study. The author also acknowledges the support of computational facility and software from the National Center for High-Performance Computing, Taiwan, ROC.

References

[1] D.J. Moon, Catalysis Surveys from Asia 12 (2008) 188–202.
[2] V. Subramani, S.K. Gangwal, Energy and Fuels 28 (2008) 814–839.
[3] A. Irankhah, A. Haghtalab, Chemical Engineering and Technology 31 (2008) 525–536.
[4] W.H. Chen, M.R. Lin, T.L. Jiang, M.H. Chen, International Journal of Hydrogen Energy 33 (2008) 6644–6656.
[5] Z. Al-Hamamrea, S. Voß, D. Trimis, International Journal of Hydrogen Energy 34 (2009) 827–832.
[6] W.H. Chen, J.G. Jheng, Journal of Power Sources 172 (2007) 368–375.

[7] W.H. Chen, J.G. Jheng, A.B. Yu, International Journal of Hydrogen Energy 33 (2008) 4789–4797.
[8] B.C. Enger, R. Lodeng, A. Holmen, Applied Catalysis A-General 346 (2008) 1–27.
[9] A.P.E. York, T.C. Xiao, M.L.H. Green, Topics in Catalyst 22 (2003) 345–358.
[10] L.W. Chen, Q. Hong, J.Y. Lin, F.M. Dautzenberg, Journal of Power Sources 164 (2007) 803–808.
[11] M. Prettre, C. Eichner, M. Perrin, Transactions of the Faraday Society 42 (1946) 335–339.
[12] A.T. Ashcroft, A.K. Cheetham, J.S. Foord, M.L.H. Green, C.P. Grey, A.J. Murrell, P.D.F. Vernon, Nature 344 (1990) 319–321.
[13] H. Horn, K.A. Williams, N.J. Degenstein, A. Bitsch-Larsen, D. Dalle Nogare, S.A. Tupy, L.D. Schmidt, Journal of Catalysis 249 (2007) 380–393.
[14] D.A. Hickman, L.D. Schmidt, Science 259 (1993) 343–346.
[15] D.A. Hickman, L.D. Schmidt, AIChE Journal 39 (1993) 1164–1177.
[16] K.A. Williams, R. Horn, L.D. Schmidt, AIChE Journal 53 (2007) 2097–2113.
[17] W. Jin, X. Gu, S. Li, P. Huang, N. Xu, J. Shi, Chemical Engineering Science 55 (2000) 2617–2625.
[18] M.E.E. Abashar, F.M. Alhabdana, S.S.E.H. Elnashaieb, International Journal of Hydrogen Energy 33 (2008) 2477–2488.
[19] R.E. Sonntag, C. Borgnakke, G.J. Van Wylen, Fundamentals of Thermodynamics, Wiley, New York, 2003.
[20] S.V. Patankar, Numerical Heat Transfer and Fluid flow, Hemisphere, Washington, DC, 1998.
[21] S.R. Turns, An Introduction to Combustion—Concepts and Applications, McGraw-Hill, New York, 2006.
[22] I. Glassman, Combustion, Academic Press, San Diego, 1996.
[23] T.L. Jiang, W.S. Chen, M.J. Tsai, H.H. Chiu, Combustion Science and Technology 102 (1994) 115–143.
[24] T.L. Jiang, W.S. Chen, M.J. Tsai, H.H. Chiu, Combustion and Flame 103 (1995) 221–238.
[25] W.H. Chen, Combustion Science and Technology 154 (2000) 229–257.
[26] W.H. Chen, Journal of Heat Transfer-Transactions of the ASME 122 (2000) 730–740.
[27] Y.C. Chao, C.Y. Wu, T. Yuan, T.S. Cheng, Combustion Science and Technology 174 (2002) 87–110.
[28] M.J. Tummers, A.W. Hubner, E.H. van Veen, K. Hanjalic, T.H. van der Meer, Combustion and Flame 156 (2009) 447–459.